PORT SAID ENGINEERING RESEARCH JOURNAL
Faculty of Engineering - Port Said University
Volume 29 No. 3 pp: 63:80

The behavior of partially encased composite steel beams subjected to flexural loads

Salah Nagy[1*], *Tarek Sharaf*[2], *and Mohammed ElGhandour*[3]

[1*] *Researcher, Department of Civil Engineering, Port Said University, Egypt, email:* engineer.sne@gmail.com
[2] *Professor, Department of Civil Engineering, Port Said University, Egypt, email:* tarek.sharaf@eng.psu.edu.eg
[3] *Professor, Department of Civil Engineering, Port Said University, Egypt, email:* dr.elghandor@gmail.com

**Corresponding author, DOI: 10.21608/pserj.2025.359254.1393*

Received 9-2-2025,
Revised 18-5- 2025,
Accepted 29-5-2025

ABSTRACT

Studying the behavior of a novel partially encased composite steel beam (PECSB) under flexural loads is the objective of this article. To improve the PECSB, the varus-equipped U-shaped steel section is joined to the slab concrete by top shear connectors and to the bottom portion by side shear connections. The Finite Element Method (FEM) was used to perform the investigation research for the experimental task. The concrete and steel coefficients of friction, which were taken from lab tests when side shear connections were used and when they weren't, were around 0.65 and 0.46, respectively. As the ultimate load approached, the slide between the concrete and steel at the end of the beam nearly reached 0.9 mm. To create safe and effective systems for both residential and commercial applications, parametric research was carried out numerically to examine how 108 FE models of PECSB with various parameters behaved under flexural loads. Observations of typical failure mechanism phases revealed that the factors improve the ultimate bending capacity. High agreement was found when the ultimate load capacity for the FEA and the theoretical findings utilizing EC4 were compared. The design specifics were proposed concerning the steel web's height-to-thickness ratio and the slab width-to-thickness ratio, which should not be greater than 130 and 10, respectively. Furthermore, it has high stability, deformability, and ductility, with mid-span deflection and ductility factors up to $L_0/13$ and 26, respectively.

Keywords: Finite Element Method, Composite Beam, Shear Connector, Slip, Parametric Research.

1. INTRODUCTION

Because it minimizes the drawbacks of concrete and steel while combining their advantages, composite building has become a popular method in many countries in recent years. The composite steel beams that are partly enclosed in concrete are poured into a U-shaped steel section to create PECSBs, a form of Composite Beam (CB) where the steel and concrete complement each other. PECSB has frequently been used in bridge and building construction because of its many benefits over conventional steel-concrete CBs, including: (1) By combining steel's high tensile strength with concrete's strong compressive strength [1,2], the CB's flexural strength is greatly increased; (2) Additionally, according to Junli et al. [3], who looked into the fire resistance of several CB types, the inside concrete may absorb heat transmitted from the external steel section, increasing the CB' fire resistance; (3) Because the encased concrete may function as a single unit with the steel section to avoid or postpone torsion or local buckling, the PECSB can achieve greater moment capacity, ductility, and high structural performance in comparison to typical beams; (4) Less welding is necessary since the U-shaped steel section's webs are rather thick and don't need many stiffeners.

Several composite section systems were added to building construction in the latter half of the 20th century. To enhance their structural qualities, a variety of profiled CB shapes have been created and studied. Bradford and Oehlers [4–7] used profiled steel sheets and infilled concrete to build composite profiled beams. To lessen creep deformation for the steel web, they experimented with the beam's flexural strength, deflection, and a small amount of dead weight. A technique for forecasting the shear resistance of spiral shear connections for CBs in plastic and elastic zones was put out by M. A. Dabaon [8]. The theoretical and experimental results for a CB with spiral shear are compared. Innovative CB designs have been developed and researched recently to reduce costs, stop some of the destructive behavior of steel girders, and get rid of the architectural difficulties associated with shear connections. Of particular significance is the U-shaped girder beam, one of the several innovative forms of CBs [9–12]. Many comparable kinds of CBs with high ductility and considerable bending strength were suggested [13–15]. Ten specimens underwent a bending test by Jiepeng et al. [16,17], who considered the following factors: beam height, shear connection degree, and tensile reinforcement ratio. Steel rebars in the shape of an inverted U are used to link the concrete slab to the bottom portion. Lastly, design information on the steel section's thickness ratio, the steel web's height-to-thickness ratio, and the longitudinal reinforcement at the bottom is recommended.

To improve composite action, the U-shaped steel section with a varus is presented in the current study. It is attached to the slab concrete by top shear connectors and to the bottom portion by side shear connectors. By altering the geometric dimensions for effective parameters, this work seeks to enhance the behavior of PECSB. This project is divided into three primary parts. The first was an inquiry study that used FEA based on earlier CB experimental work. [16]. In the second phase, 108 (3D) models were parametrically investigated by (FEM) with varying effective factors such as slab thickness, side shear connections, the section height, beam width, and steel section thickness. To get a satisfactory reaction, material laboratory investigations were conducted to determine the ideal coefficient of friction between concrete and steel plates. The final stage contrasts the FEA method's ultimate load result with the theoretical approach as per EC4 [18].

2. NUMERICAL INVESTIGATION

For experimental work utilizing the FEA approach, a verification study was conducted. The behavior of the CB section in the experimental test was simulated and predicted using the ABAQUS® finite element software. FEA and the experimental results of Jiepeng et al. [16] were contrasted. Good agreement was found between the FEA results and the results of the actual testing of the load-deflection relationship and failure modes that occurred for the specimens under examination. Additionally, it was seen that the FEA technique saves time and money while producing accurate results when compared to experimental work.

2.1 Model description

Jiepeng et al. [16] investigated a cold-formed U-shaped steel-concrete CB reinforced with a rebar truss. The T-shaped, simply supported CB that made up each specimen had the following measurements: $f_{cu,k}$ (compressive strength of the cubic concrete) = 45 MPa, t_b (thickness of the concrete slab) = 100 mm, t_w (thickness of the U-shaped steel section) 4 mm, and b (width of the lower part) = 150 mm. During the experiments, both HRB400 and Q235B were utilized as reinforcement and structural steel. The protective layer thickness of the ribbed reinforcement in the concrete slab (a) is 20 mm, and the beam depths (H) of 350 and 450 mm are taken into account.

2.2 Finite Element Model

For the experimental specimens, three-dimensional (FE) models were simulated using the FE analysis. The concrete is meshed using the eight-node solid element in three dimensions with reduced integration (C3D8R), while the U steel section was meshed using the four-node shell element with reduced integration (S4R). The reinforcement is made of (T3D2) truss elements, while the shear connections are made of (CONN3D2). A mesh 25 mm deep can yield dependable results, as seen in figure 1. A range of mesh sizes was investigated to find an appropriate mesh that offers accurate results and shorter computation times. A friction coefficient of around 0.35 was what we expected.

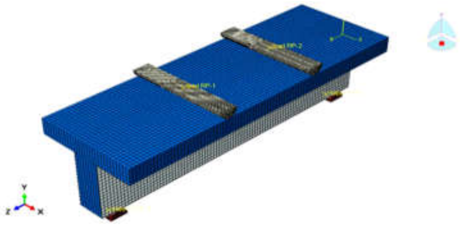

Figure 1: 3D Model [16]

2.3 Results and Discussion

2.3.1 Curves of load-deflection

Figure 2 compares the load-deflection curves of the experimental specimens [16] with the results of the FEA. A 2-point symmetrical bending moment delivered from a distribution beam served as the fundamental support for each specimen under examination. During the elastic stage, a loading rate of 3 kN/min was applied for each 50 kN increase in load. The loading procedure was adjusted at an increasing rate of 0.8 mm/min when the steel soffit gave way. During the decline period, the load is 85% of its maximum load. In each picture, there is a good correspondence between the curves obtained from the FEA and those obtained from experimental tests. Furthermore, it is noted that for every specimen that the experimental and FEA findings correspond well with the beginning range of loading in the load-deflection relation. To determine the ideal mesh size, several experiments were carried out. Last but not least, the outcomes of employing an intermediate-size mesh can yield excellent results with respectable accuracy, data storage capacity, and computation run time.

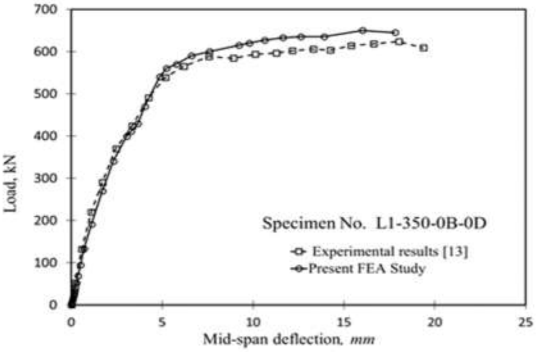

(a)

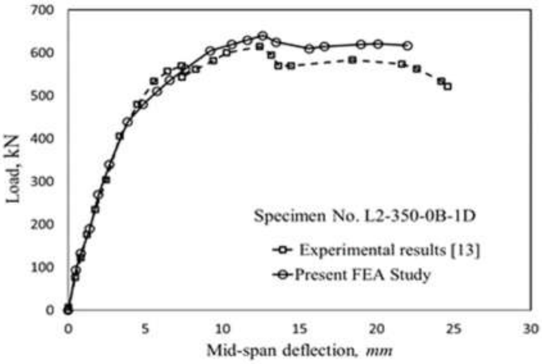

(b)

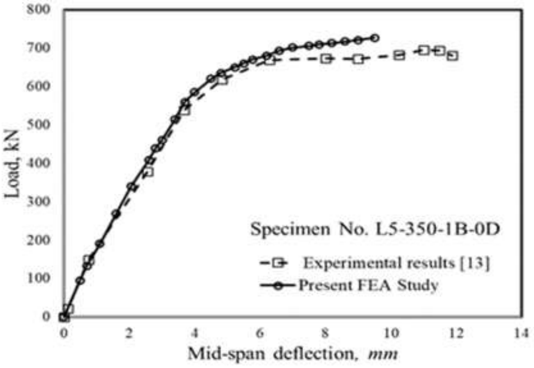

(c)

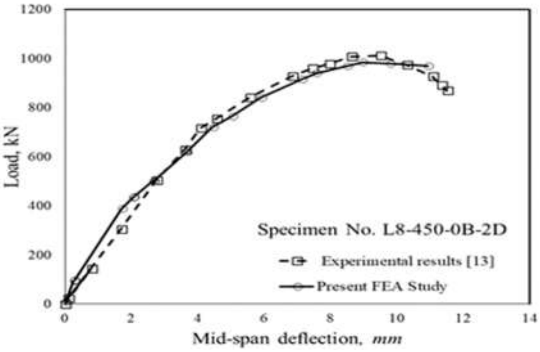

(d)

Figure 2: Comparison between FE results and experimental specimens [16]

2.3.2 Failure modes

The failure modes of the experimental specimens [16] and those derived from the FEA are contrasted in figure 3. Because the causes of the failures in both cases are identical, the failure modes and distorted forms of failure that were generated by both tests and FEA are comparable. Under certain circumstances, the specimens exhibit four failure modes: for model L1 figure 3a, longitudinal slip failure happens when tensile reinforcement is lacking and the full shear connection cannot be achieved, whereas, for model L2 figure 3b, slip and local buckling failure of the steel web occurs. Whether the beam has a complete shear connection or meticulous longitudinal tensile reinforcing, both failures can happen. The purpose of this study is to compare the experimental findings of Jiepeng [16] with the FEA results of the FE analysis. These findings included the load-deflection curves and the failure mechanisms. There is a little variation of up to 5% between the experimental and FEA results. This is because the idealized material stress-strain curve for FEA differs from the actual material stress-strain curve for testing. Furthermore, a geometric discrepancy in dimensions between numerical and physical models is caused by manufacturing flaws as well as flaws in test components.

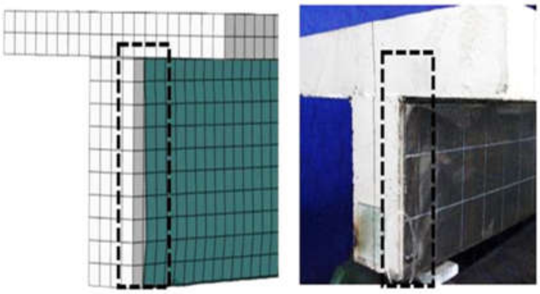

a. L1 Longitudinal slip failure

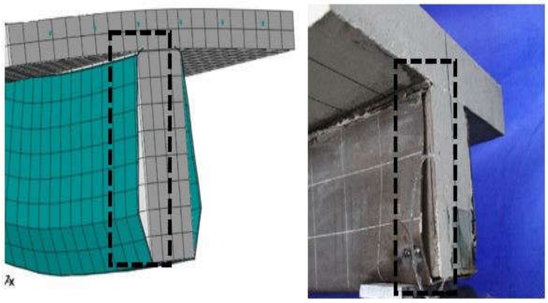

b. L2 Slip and local buckling failure of the steel web

Figure 3: Comparison between ultimate failure modes for specimens L1 and L2.

3. PARAMETRIC STUDY

As seen in figures 4a and 4b, a parametric analysis was conducted to create 3D-FE models of PECSB with various parameters. The purpose of this study is to ascertain how these effective characteristics affect the ultimate moment capacity and to comprehend how PECSB behaves under flexural loads.

3.1 Model description

To examine the behavior of PECSB under flexural loads, 108 3D-FE models of the beams were produced using the FE analysis. The characteristics and size of the models used in the parametric investigation are listed in table 1. Slab width (B) = 1000 mm, section height (H) = 400, 500, and 600 mm, beam width (b) = 150, 200, and 250 mm, slab thickness t_s = 80, 100, and 120 mm, U-shaped steel section thickness t_w = 2 and 4 mm, and total length (L) = 3000 mm are the dimensions of these models. The slab's reinforcing bars are made of a single-layer mesh with a bar diameter of 12 mm spaced 200 mm apart in the x and z axes. The side shear connectors (SSC), which are arranged in two rows on either side of the steel section, were only used in half of the models and were denoted as (W-SSC), while the other was (W/O-SSC).). This means (With Side Shear Connectors) and (Without Side Shear Connectors. The shear connectors used in this study were positioned every 100 mm as shear studs of Φ16 mm diameter and a height of 50 mm at the top of the steel section for all cases.

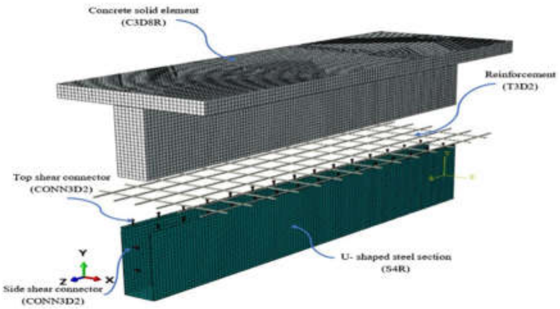

a. Typical 3D model and FE mesh of the PECSB.

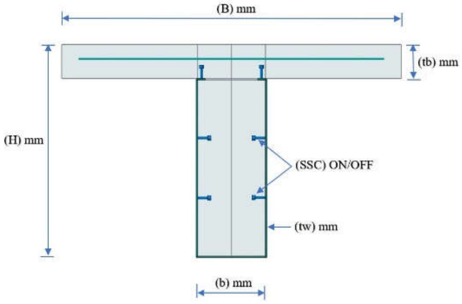

b. Cross-section of PECSB

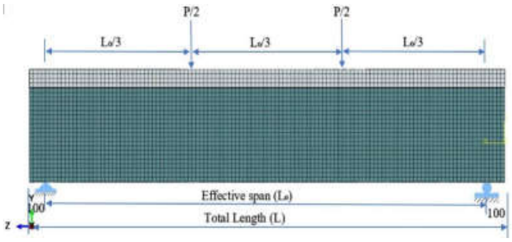

c. Boundary conditions for a typical model

Figure 4: Composite Beam

Table 1. The parameters and dimensions of PECSB were used in the parametric study.

Section Height (H)mm	Beam Width (b)mm	Slab Thickness (t_s) mm	Web Thickness (t_w) mm	Side Shear Connectors (SSC)
400	150	80	2	W-SSC
500	200	100	4	W/O-SSC
600	250	120		

3.1.1 Material modelling

3.1.1.1 Steel plates, rebars, and shear connectors

To ascertain the material qualities of the U-shaped steel plates with thicknesses of 2 mm and 4 mm as well as steel reinforcing bars, standard tension coupon tests were carried out per ASTMA370 [19]. The average outcomes of these tests are presented in table 2. The steel components have a density of 7850 kg/m3 and Poisson's ratio equals to 0.3. A tri-linear stress-strain relation curve representing the general constitutive laws used to determine the stress-strain characteristics of the U-shaped steel plates is shown in figure 5a. The stress-strain curve is defined by the yield strength of steel plates (f_{ys}), the yield strain (ε_{ys}), and the ultimate strength fus, whereas the strain ε_{ts} at the start of strain hardening and the ultimate strain limit ε_{us} were assumed to be 0.025 and 0.25 respectively. Additionally, a simple elastic-perfectly-plastic model without strain hardening behavior is used for the steel reinforcing bars, with yield strength and ultimate strength calculated to be 376 MPa and 460 MPa, respectively. As seen in figure 5, the bi-linear stress-strain curve put out by Loh et al. [20] was utilized to model the material characteristics of the shear connections. b with a 785 MPa maximum tensile strength.

3.1.1.2 Concrete

Table 2 states the concrete material characteristics employed in the models, including its elastic modulus and typical strength. Using ECP 203-2020 [21], six standard concrete cubes 150×150×150 mm were evaluated after 28 days. The concrete's stress-strain failure curve is displayed in figure 5c. According to the hypothesis of Du et al. [22], the concrete damage plasticity was used in the FE analysis to simulate the nonlinear behavior of concrete. The concrete plastic technique is used to define the concrete damage variables, and five parameters define the yield function: A ratio of initial uniaxial compressive yield stress to initial uniaxial compressive yield stress is 1.16, the second stress invariant on the tensile meridian (K) is 0.1, the dilation angle (ψ) is 30°, and eccentricity (e) is 0.6667, and viscosity parameter (ν) is 0.005.

Table 2. Measured material properties.

Material	Diameter/ Thickness (mm)	Yield Strength (MPa)	Ultimate Strength (MPa)	Elastic Modulus (MPa)
Steel	2	326	425	194000
	4	330	430	198140
Reinforcement	Φ 12	376	460	200000
Shear connector	Φ 16	-	785	-
Concrete	-	-	43	30934

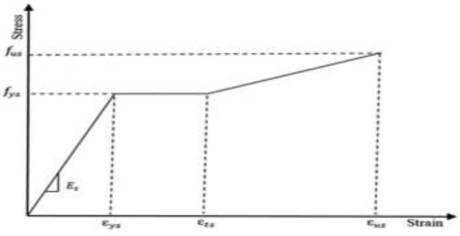

a. Stress-strain curve of U-shaped steel plates

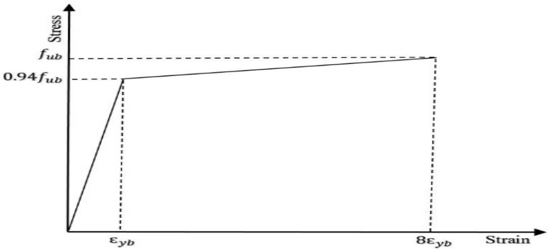

b. Stress-strain curve of shear connectors

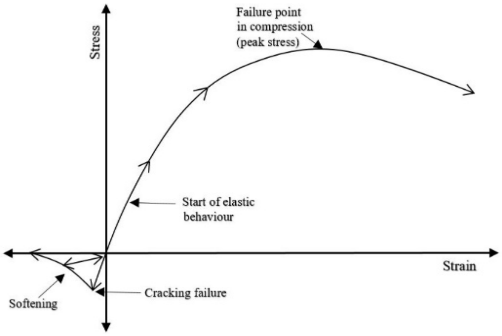

c. Stress-strain curve of concrete

Figure 5: Stress-strain curve for concrete and steel parts

3.1.2 Friction between steel and concrete

To find the coefficient of friction between concrete and steel, whether side shear connections were used or not, experimental tests were conducted on both square and circular specimens. As seen in figure 6, the use of a compressive machine separates the steel-concrete bond by 0.6 MPa/sec. At 0.41 MPa, the specimens' normal stresses remained unchanged [23]. The coefficient of friction is calculated by dividing the continuous normal stresses by the shear stress values necessary to induce the initial slide.

Figure 6. Test setup

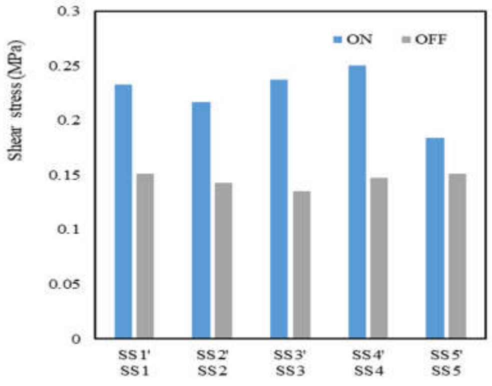

a. Square Specimens

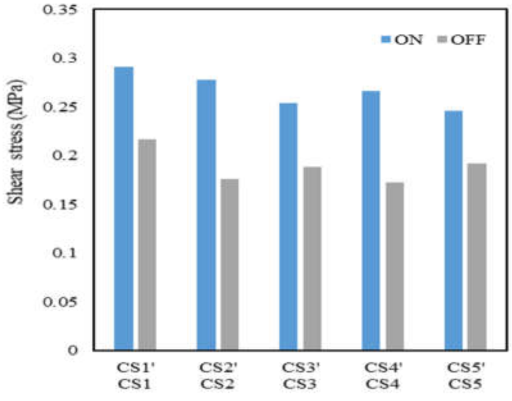

b. Circular Specimens

Figure 7: Comparison between square specimens and circular specimens when using side shear connectors or not.

The values of the coefficient of friction between concrete and steel are shown in figure 7. The side shear connections for square specimens ranged from 0.53 to 0.61, with an average of 0.54. When side shear connections were not used, the coefficient of friction values for square specimens ranged from 0.33 to 0.37, with an average of 0.35, as seen in figure 7a. Additionally, as illustrated in figure 7b, the coefficient of friction values for circular specimens when side shear connectors were used ranged from 0.6 to 0.71 and were averaged at 0.65, whereas the coefficient of friction values for circular specimens when side shear connectors were not used ranged from 0.42 to 0.53 and were averaged at 0.46. Numerical evaluations of the models that will be examined in the parametric research will make use of the coefficient of friction values between steel and concrete that were taken from laboratory trials.

3.2 Finite Element Model

A U-shaped steel section, concrete, reinforcement, and shear connections were among the pieces that made up PECSB. The (FE) components of the models were constructed and put together using the FE analysis. As seen in figure 4a, the concrete was meshed with an eight-node solid element in three dimensions (3D) with reduced integration (C3D8R), while the U-shaped steel section was meshed with a four-node shell element with reduced integration (S4R). The reinforcement was meshed using (T3D2) (3D) using a 2-node truss element, and the connector element for shear connections was (CONN3D2) 2-node (3D). The mesh chosen for the numerical research was 25 mm deep. The head of the shear connections and the reinforcements were inserted in the concrete, and the U-shaped steel section and shear connectors were connected as one cohesive unit. A surface-to-surface contact type with friction and no penetration in the normal and tangential directions, respectively, is present at the interface between the concrete and the U-shaped steel section. According to earlier experimental work, the coefficient of friction between the concrete and the steel plates was around 0.65 when side shear connections were used and 0.46 when they weren't. The boundary conditions were performed as simply supported end conditions with four-point bending when loaded with two-point loads at $L_0/3$ of the bend, as shown in figure 4c.

3.3 Results and Discussion

Table 3 summarizes the results of 108 FE partially encased composite steel beams PECSB obtained from the parametric study such as yield load (P_y), ultimate load (P_u), yield deflection (δy), deflection corresponds to 85% of the peak load while at the stage declines (δf), ductility factor (μ), and various types of failure modes.

3.3.1 Failure modes

The following characteristics of the FEA study's various failure modes for PECSB are depicted in figure 8 (1) The majority of the materials that make up PECSB reach their maximum strength before the peak load; (2) The composite action between the concrete and steel diminishes, and shear failure takes place between the encased concrete and the U-shaped steel section following the ultimate load.

The encased concrete and the slab concrete in PECSB are a single unit during the first loading process for the models (008 H400 b200 t_s80 t_w2 W/O-SSC) and (103 H600 b250 t_s80 t_w4 W-SSC). The entire composite action in the neck zone could not be achieved by increasing the load because the top shear connections were insufficient to withstand the uplift stress. As a result, as seen in figures 8 a and 8e, there was vertical uplift failure at the weak neck zone between the concrete slab and the top beam due to local buckling of the steel web, top flange failure, and top shear connection failure. It may be inferred that over the shear span, the uplift force rises from the loading point to the beam end. Even though PECSB's concrete is a monolithic unit, it is insufficient to provide a complete shear connection between the top beam and the concrete slab at the neck zone. Therefore, we may raise the thickness of the slab, increase the steel ratio for top shear connectors, and install an appropriate anti-uplift bar to prevent any uplift failures to improve the weak zone between the slab and the bottom section.

As seen in figure 8f and 8b, oblique shear cracks developed on the sides of the encased concrete, and concrete slab crushing occurred for the models (010 H400 b200 t_s100 t_w2 W/O-SSC) and (105 H600 b250 t_s100 t_w4 W-SSC) following the yielding and removal of the exterior U-shaped steel section. These cracks are caused by the act of shear forces and the low steel ratio of side shear connectors for the large depth. Therefore, the slab width-to-thickness ratio should not be greater than 10 to increase the slab's concrete strength. There were no side shear connectors for the model (016 H400 b250 t_s100 t_w2 W/O-SSC) during the initial loading procedure, and the steel web's low steel ratio resulted in local The slide is minor and manageable, although there is buckling in the steel web. It rose more quickly and was unable to accomplish full composite action between the concrete and the U-shaped steel portion because the top shear connections were insufficient to prevent the slide. Ultimately, as seen in figure 8c, the model failed because the U-shaped steel and the enclosed concrete functioned independently. During the first loading operation, the model (099 H600 b200 t_s100 t_w4 W-SSC) remained a single unit. Following that, it was seen that the steel web experienced local buckling as a result of its great depth, and that side shear connections gave way as the load increased. Lastly, the model fails as seen in figure 8d because a tiny steel ratio inside shear connections is unable to prevent the slide between the encased concrete and the U-shaped steel section.

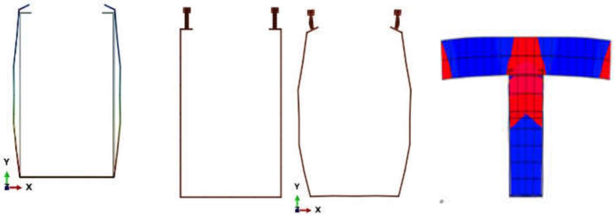
1-Top flange and web local buckling

2-Top shear connector failure

3-Vertical uplift failure

a. 008 H400 b200 t_s80 t_w2 W/O-SSC

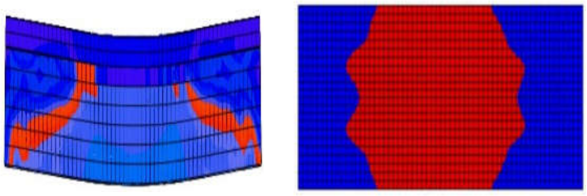
1-Oblique shear crack

2-Concrete slab crushing

b. 010 H400 b200 t_s100 t_w2 W/O-SSC

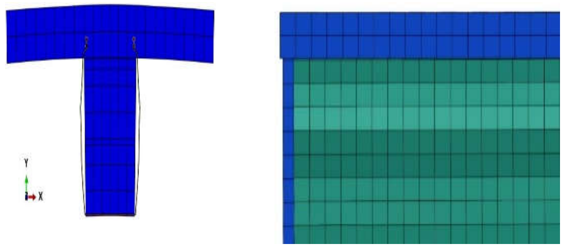
1-Local buckling steel web, then top shear connector failure

2- Longitudinal slip failure

c. 016 H400 b250 t_s100 t_w2 W/O-SSC

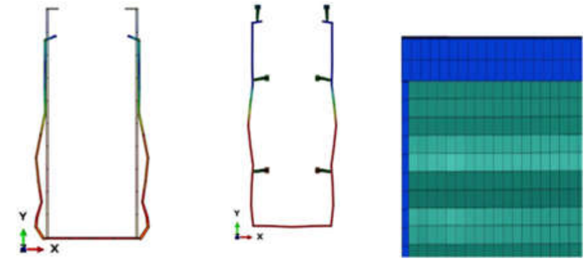
1-Local buckling of steel web

2-Side shear connector failure

3- Longitudinal slip failure

d. 099 H600 b200 t_s100 t_w4 W-SSC

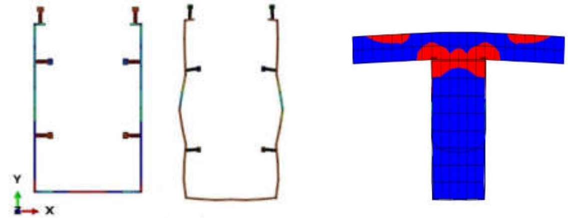
1-Top flange local buckling and top shear connector failure

2-Vertical uplift failure

e. 103 H600 b250 t_s80 t_w4 W-SSC

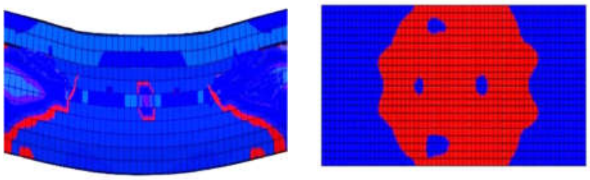
1-Oblique shear crack

2- Concrete slab crushing

f. 105 H600 b250 t_s100 t_w4 W-SSC

Figure 8: Failure modes for the models 008, 010, 016, 099, 103, and 105.

Table 3. Yield load (P_y), ultimate load (P_u), yield deflection(δy), deflection corresponding to 85% peak load(δf), ductility factor(μ), and failure modes for the 108 FE models.

Model Label	P_y (kN)	P_u (kN)	δy (mm)	δf (mm)	μ	Failure Modes
001 H400 b150 t_s80 t_w2 W-SSC	225	270	5.2	94.6	18.2	OSC+CSC
002 H400 b150 t_s80 t_w2 W/O-SSC	219	269	5	90	18	LBSW+TSCF+LSF
003 H400 b150 t_s100 t_w2 W-SSC	227	280	5.1	93.3	18.3	LBSW+SSCF+LSF
004 H400 b150 t_s100 t_w2 W/O-SSC	222	275	5	91	18.2	LBSW+TSCF+LSF
005 H400 b150 t_s120 t_w2 W-SSC	230	290	5.3	97	18.3	TFLB+TSCF+VUF
006 H400 b150 t_s120 t_w2 W/O-SSC	225	285	5.1	92.3	18.1	TFLB+TSCF+VUF
007 H400 b200 t_s80 t_w2 W-SSC	227	325	5.2	96.2	18.5	TFLB+TSCF+VUF
008 H400 b200 t_s80 t_w2 W/O-SSC	221	322	5	92	18.4	TFLB+TSCF+VUF
009 H400 b200 t_s100 t_w2 W-SSC	266	360	5.9	100	18.5	OSC+CSC
010 H400 b200 t_s100 t_w2 W/O-SSC	264	354	5.3	101	19.2	OSC+CSC
011 H400 b200 t_s120 t_w2 W-SSC	268	404	5.5	102.3	18.6	LBSW+SSCF+LSF
012 H400 b200 t_s120 t_w2 W/O-SSC	267	395	5.4	99.4	18.4	LBSW+TSCF+LSF
013 H400 b250 t_s80 t_w2 W-SSC	285	405	5.4	101.5	18.8	LBSW+SSCF+LSF
014 H400 b250 t_s80 t_w2 W/O-SSC	280	385	5.3	98	18.5	TFLB+TSCF+VUF
015 H400 b250 t_s100 t_w2 W-SSC	325	432	5.5	103.4	18.8	LBSW+TSCF+LSF
016 H400 b250 t_s100 t_w2 W/O-SSC	320	411	6.3	108	17.1	LBSW+TSCF+LSF
017 H400 b250 t_s120 t_w2 W-SSC	328	421	5.6	106.4	19	LBSW+TSCF+LSF
018 H400 b250 t_s120 t_w2 W/O-SSC	325	409	5.5	103.4	18.8	LBSW+TSCF+LSF
019 H500 b150 t_s80 t_w2 W-SSC	331	430	5.7	108.3	19	OSC+CSC
020 H500 b150 t_s80 t_w2 W/O-SSC	328	400	5.4	102	18.9	OSC+CSC
021 H500 b150 t_s100 t_w2 W-SSC	336	437	5.6	108	19.3	TFLB+TSCF+VUF
022 H500 b150 t_s100 t_w2 W/O-SSC	330	412	5.6	106.4	19	TFLB+TSCF+VUF
023 H500 b150 t_s120 t_w2 W-SSC	348	487	5.7	110	19.3	LBSW+TSCF+LSF
024 H500 b150 t_s120 t_w2 W/O-SSC	341	448	5.6	107	19.1	LBSW+TSCF+LSF
025 H500 b200 t_s80 t_w2 W-SSC	364	500	5.8	112.5	19.4	TFLB+TSCF+VUF
026 H500 b200 t_s80 t_w2 W/O-SSC	355	460	5.7	109.4	19.2	TFLB+TSCF+VUF
027 H500 b200 t_s100 t_w2 W-SSC	360	551	5.8	113.1	19.5	OSC+CSC

Table 3. Continued

Model Label	P_y (kN)	P_u (kN)	δy (mm)	δf (mm)	μ	Failure Modes
028 H500 b200 t_s100 t_w2 W/O-SSC	357	530	5.7	110.6	19.4	OSC+CSC
029 H500 b200 t_s120 t_w2 W-SSC	389	615	5.8	113.1	19.5	LBSW+SSCF+LSF
030 H500 b200 t_s120 t_w2 W/O-SSC	370	580	5.6	109.7	19.3	LBSW+TSCF+LSF
031 H500 b250 t_s80 t_w2 W-SSC	446	650	5.8	113.7	19.6	LBSW+SSCF+LSF
032 H500 b250 t_s80 t_w2 W/O-SSC	438	620	5.5	106.7	19.4	LBSW+TSCF+LSF
033 H500 b250 t_s100 t_w2 W-SSC	467	653	5.9	116.8	19.8	TFLB+TSCF+VUF
034 H500 b250 t_s100 t_w2 W/O-SSC	459	650	5.8	113.7	19.6	TFLB+TSCF+VUF
035 H500 b250 t_s120 t_w2 W-SSC	532	660	6	120	20	LBSW+SSCF+LSF
036 H500 b250 t_s120 t_w2 W/O-SSC	517	648	5.8	114.8	19.8	LBSW+TSCF+LSF
037 H600 b150 t_s80 t_w2 W-SSC	538	673	6	123	20.5	LBSW+SSCF+LSF
038 H600 b150 t_s80 t_w2 W/O-SSC	521	660	5.9	116.8	19.8	OSC+CSC
039 H600 b150 t_s100 t_w2 W-SSC	540	671	6	123.6	20.6	OSC+CSC
040 H600 b150 t_s100 t_w2 W/O-SSC	535	663	5.8	113.1	19.5	OSC+CSC
041 H600 b150 t_s120 t_w2 W-SSC	546	690	6.2	122.7	19.8	LBSW+SSCF+LSF
042 H600 b150 t_s120 t_w2 W/O-SSC	540	696	6	117	19.5	LBSW+ TSCF+LSF
043 H600 b200 t_s80 t_w2 W-SSC	559	698	6.3	131	20.8	LBSW+SSCF+LSF
044 H600 b200 t_s80 t_w2 W/O-SSC	556	681	6.1	125	20.5	LBSW+TSCF+ LSF
045 H600 b200 t_s100 t_w2 W-SSC	563	708	6.3	132.3	21	OSC+CSC
046 H600 b200 t_s100 t_w2 W/O-SSC	559	702	6.2	128.3	20.7	LBSW+TSCF+LSF
047 H600 b200 t_s120 t_w2 W-SSC	570	713	6.5	139.7	21.5	LBSW+SSCF+LSF
048 H600 b200 t_s120 t_w2 W/O-SSC	563	710	6.3	132.3	21	LBSW+TSCF+LSF
049 H600 b250 t_s80 t_w2 W-SSC	540	738	6.6	144.5	21.9	OSC+CSC
050 H600 b250 t_s80 t_w2 W/O-SSC	535	734	6.5	139.8	21.5	OSC+CSC
051 H600 b250 t_s100 t_w2 W-SSC	538	766	6.7	147.4	22	LBSW+SSCF+LSF
052 H600 b250 t_s100 t_w2 W/O-SSC	530	760	6.5	141.7	21.8	LBSW+TSCF+LSF
053 H600 b250 t_s120 t_w2 W-SSC	575	782	6.6	148.5	22.5	LBSW+SSCF+LSF
054 H600 b250 t_s120 t_w2 W/O-SSC	565	766	6.5	145	22.3	LBSW+TSCF+LSF

Table 3. Continued

Model Label	P_y (kN)	P_u (kN)	δy (mm)	δf (mm)	μ	Failure Modes
055 H400 b150 t_s80 t_w4 W-SSC	426	523	6.7	151.4	22.6	OSC+CSC
056 H400 b150 t_s80 t_w4 W/O-SSC	420	514	6.5	144.3	22.2	LBSW+TSCF+LSF
057 H400 b150 t_s100 t_w4 W-SSC	442	581	6.7	152.7	22.8	LBSW+SSCF+LSF
058 H400 b150 t_s100 t_w4 W/O-SSC	390	550	6.6	148.5	22.5	LBSW+TSCF+LSF
059 H400 b150 t_s120 t_w4 W-SSC	499	644	6.8	156.4	23	TFLB+TSCF+VUF
060 H400 b150 t_s120 t_w4 W/O-SSC	495	630	6.6	149.1	22.6	TFLB+TSCF+VUF
061 H400 b200 t_s80 t_w4 W-SSC	527	689	6.8	158.4	23.3	TFLB+TSCF+VUF
062 H400 b200 t_s80 t_w4 W/O-SSC	506	670	6.5	150.1	23.1	TFLB+TSCF+VUF
063 H400 b200 t_s100 t_w4 W-SSC	530	696	6.7	157.4	23.5	OSC+CSC
064 H400 b200 t_s100 t_w4 W/O-SSC	522	692	6.6	153.7	23.3	OSC+CSC
065 H400 b200 t_s120 t_w4 W-SSC	644	843	6.8	161.1	23.7	OSC+CSC
066 H400 b200 t_s120 t_w4 W/O-SSC	621	807	6.7	157.4	23.5	LBSW+TSCF+LSF
067 H400 b250 t_s80 t_w4 W-SSC	625	774	6.8	162.5	23.9	LBSW+TSCF+LSF
068 H400 b250 t_s80 t_w4 W/O-SSC	623	761	6.7	158.1	23.6	LBSW+TSCF+LSF
069 H400 b250 t_s100 t_w4 W-SSC	630	781	6.9	162.8	23.8	TFLB+TSCF+VUF
070 H400 b250 t_s100 t_w4 W/O-SSC	627	772	6.8	160.5	23.6	LBSW+TSCF+LSF
071 H400 b250 t_s120 t_w4 W-SSC	671	943	7	168	24	LBSW+TSCF+LSF
072 H400 b250 t_s120 t_w4 W/O-SSC	660	920	6.8	161.8	23.8	LBSW+TSCF+LSF
073 H500 b150 t_s80 t_w4 W-SSC	550	755	7	168.7	24.1	LBSW+TSCF+LSF
074 H500 b150 t_s80 t_w4 W/O-SSC	547	740	6.9	164.9	23.9	OSC+CSC
075 H500 b150 t_s100 t_w4 W-SSC	568	760	7.2	174.2	24.2	TFLB+TSCF+VUF
076 H500 b150 t_s100 t_w4 W/O-SSC	550	741	6.8	163.2	24	TFLB+TSCF+VUF
077 H500 b150 t_s120 t_w4 W-SSC	570	870	7.2	175.7	24.4	LBSW+TSCF+LSF
078 H500 b150 t_s120 t_w4 W/O-SSC	561	855	6.9	166.3	24.1	LBSW+TSCF+LSF
079 H500 b200 t_s80 t_w4 W-SSC	670	890	7.3	178.9	24.5	TFLB+TSCF+VUF
080 H500 b200 t_s80 t_w4 W/O-SSC	660	840	7.1	171.8	24.2	TFLB+TSCF+VUF
081 H500 b200 t_s100 t_w4 W-SSC	716	1036	7.3	178.9	24.5	OSC+CSC

Table 3. Continued

Model Label	P_y (kN)	P_u (kN)	δy (mm)	δf (mm)	μ	Failure Modes
082 H500 b200 t_s100 t_w4 W/O-SSC	703	1002	7.1	172.5	24.3	OSC+CSC
083 H500 b200 t_s120 t_w4 W-SSC	715	1083	7.3	179.6	24.6	LBSW+SSCF+LSF
084 H500 b200 t_s120 t_w4 W/O-SSC	706	1050	7	170.8	24.4	LBSW+TSCF+LSF
085 H500 b250 t_s80 t_w4 W-SSC	750	1058	7.3	181	24.8	LBSW+SSCF+LSF
086 H500 b250 t_s80 t_w4 W/O-SSC	740	1054	7.1	174.6	24.6	LBSW+TSCF+LSF
087 H500 b250 t_s100 t_w4 W-SSC	770	1110	7.5	185.2	24.7	TFLB+TSCF+VUF
088 H500 b250 t_s100 t_w4 W/O-SSC	761	1084	7.3	165	22.6	TFLB+TSCF+VUF
089 H500 b250 t_s120 t_w4 W-SSC	773	1130	7.5	186	24.8	LBSW+SSCF+LSF
090 H500 b250 t_s120 t_w4 W/O-SSC	769	1115	7.4	181.3	24.5	LBSW+TSCF+LSF
091 H600 b150 t_s80 t_w4 W-SSC	780	1133	7.6	190	25	LBSW+SSCF+LSF
092 H600 b150 t_s80 t_w4 W/O-SSC	775	1109	7.5	186.7	24.9	LBSW+TSCF+LSF
093 H600 b150 t_s100 t_w4 W-SSC	783	1137	7.6	191.5	25.2	LBSW+SSCF+LSF
094 H600 b150 t_s100 t_w4 W/O-SSC	777	1117	7.4	185	25	LBSW+TSCF+LSF
095 H600 b150 t_s120 t_w4 W-SSC	781	1206	7.7	193.3	25.1	LBSW+SSCF+LSF
096 H600 b150 t_s120 t_w4 W/O-SSC	779	1183	7.5	186	24.8	LBSW+TSCF+LSF
097 H600 b200 t_s80 t_w4 W-SSC	785	1233	7.8	197.4	25.3	TSCF+LSF LBSW+SSCF+LSF
098 H600 b200 t_s80 t_w4 W/O-SSC	781	1213	7.6	190.7	25.1	TFLB+TSCF+VUF
099 H600 b200 t_s100 t_w4 W-SSC	800	1337	7.8	198.9	24.4	LBSW+SSCF+LSF
100 H600 b200 t_s100 t_w4 W/O-SSC	795	1288	7.5	189.7	25.3	TFLB+TSCF+VUF
101 H600 b200 t_s120 t_w4 W-SSC	850	1390	7.9	203.8	25.8	LBSW+SSCF+LSF
102 H600 b200 t_s120 t_w4 W/O-SSC	840	1347	7.8	198.9	25.5	LBSW+TSCF+LSF
103 H600 b250 t_s80 t_w4 W-SSC	1093	1413	8	207.2	25.9	TFLB+TSCF+VUF
104 H600 b250 t_s80 t_w4 W/O-SSC	1103	1397	7.6	195.32	25.7	LBSW+TSCF+LSF
105 H600 b250 t_s100 t_w4 W-SSC	1106	1451	9	208	23.2	OSC+CSC
106 H600 b250 t_s100 t_w4 W/O-SSC	1104	1435	7.7	197.8	25.7	LBSW+TSCF+LSF
107 H600 b250 t_s120 t_w4 W-SSC	1116	1464	9	208	26	LBSW+SSCF+LSF
108 H600 b250 t_s120 t_w4 W/O-SSC	1105	1454	7.8	201	25.8	LBSW+TSCF+LSF

LSF=longitudinal slip failure, VUF=vertical uplift failure, LBSW=local buckling steel web, OSC= oblique shear crack, CSC=concrete slab crushing, SSCF=side shear connector failure, TSCF=top shear connector failure

.

3.3.2 Load-deflection relationship

Figures 9a and 9b compare the load-deflection curves of the six models, which are divided into two groups based on the section height H (400 and 600 mm). When loaded to the falling stage, all PECSBs exhibit comparatively high levels of ductility and deformability. As demonstrated in models (016 H400 b250 t_s100 t_w2 W/O-SSC) and (105 H600 b250 t_s100 t_w4 W-SSC), increasing the section height from 400 to 600 mm was found to enhance moment capacity by almost 65%. The external U-shaped steel plates are crucial for strength and ductility. The PECSB's stiffness and bearing capacity would increase if the steel thickness was increased from 2 mm to 4 mm. The groups with a 2 mm thickness of steel U-shaped section for models (No. 008, 010, and 016) saw a faster decrease in loads due to the low steel ratio than the groups with a 4 mm thickness of steel U-shaped section for models (No. 099, 103, and 105), as illustrated in figure 9a. By examining the declining phases of the curves for the two groups, this was found. The load-deflection curves demonstrate that the encased concrete and the U-shaped steel section worked in tandem when the side shear connections at the steel U-section for models (No. 099, 103, and 105) were provided. Additionally, they decreased the amount of sliding between them, and it was discovered that the top shear connections were a helpful component for fortifying the weak neck area. The loading process can be broken down into four stages using the model (103 H600 b250 t_s80 t_w4 W-SSC) in figure 9b as an example. (1) The elastic stage was defined by the linear relationship of loads and mid-span deflections because the shear connectors, external U-shaped steel section, and concrete all functioned monolithically with good composite action. Failure modes were not readily apparent at this point; (2) the steel's strain reached 0.0016 and the mid-span deflection was 7.9 mm when the load hit 1000 kN ($0.7P_u$), (3) When the load rose to 1344 kN ($0.96P_u$), the steel reached the plastic hardening stage; the mid-span deflection was 59 mm, and the U-shaped steel section produced substantial nonlinearity. The model entered the elastic-plastic stage with little nonlinearity. The concrete subsequently developed transverse fractures, and the deflection rose faster than the load; (4) the mid-span deflection was 75 mm with more deformation than in the early phases when the model reached the 1413 kN (P_u) peak load. The load then steadily decreased while the deflection rapidly grew. When the mid-span deflection finally reached $L_0/13$, the concrete started to deteriorate.

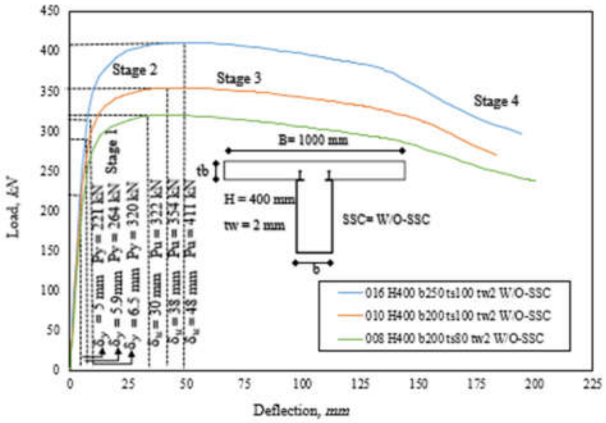

a. Load-deflection curves for models 8, 10, and 16.

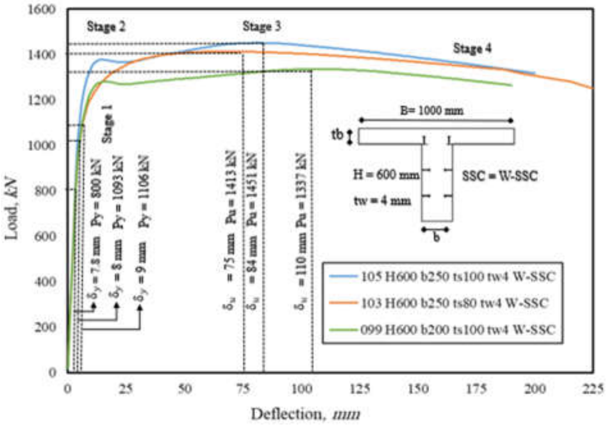

b. Load-deflection curves for models 99, 103, and 105.

Figure 9: Load-deflection curves

3.3.3 Load-strain and strain distributions relationship

All component materials reach their maximum strength before the PECSB reaches its maximum value, indicating that the CB makes full use of the material strengths and that high-strength materials may find practical use. The load-strain curves acquired at the upper center of the concrete slab are shown in figure 10a. The concrete slab for models 090, 092, 093, 094, and 099 was undamaged before the models failed Additionally, the load-strain curves for the steel section's bottom center are shown in figure 10b. At the final condition, the steel strain was approximately 0.022, and the yield strain was 0.0016. For the model (103 H600 b250 t_s80 t_w4 W-SSC), the longitudinal strain distribution along the PECSB depth at the mid-span cross-section is shown in figure 11. Note that the model operated monolithically and that there was no longitudinal sliding during the elastic zone as the external force increased. Additionally, the concrete slab deforms evenly and the strain distribution is almost linear up to a high loading level of around 78% of the ultimate load. The shear lag phenomenon, which causes the concrete slab to develop fractures, then causes the strain at the top surface in the middle of the slab to grow greater than the strain at the edge. The strain at the top surface in the middle of the concrete slab is 46% more than the edge strain when the load reaches Pu. Before the slab bottom cracking, the shared NA remained steady for the strain distribution along the beam depth. The slide started when the concrete and steel section bond split when the steel yielded at around $0.6P_u$. However, the plastic area of the steel section continuously developed until it reached the top flanges when the load reached $0.96P_u$. The same bending curve was shown by the two straight lines produced by the steel web strain and slab side strain, respectively, when the load reached P_u.

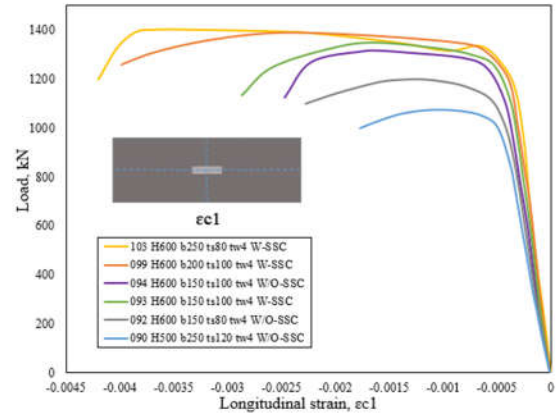

a.The top center of the concrete

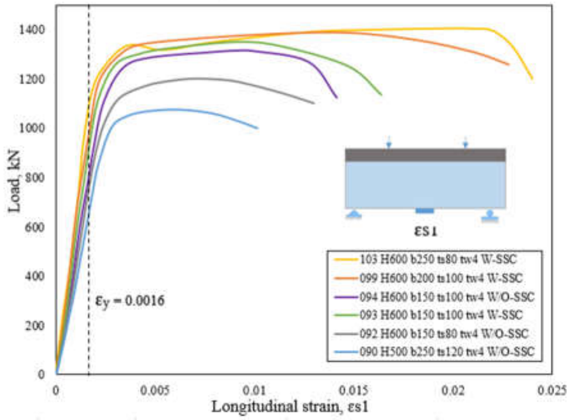

b.The bottom center of the steel section

Figure 10: The load-strain curves for the concrete slabs and the steel sections

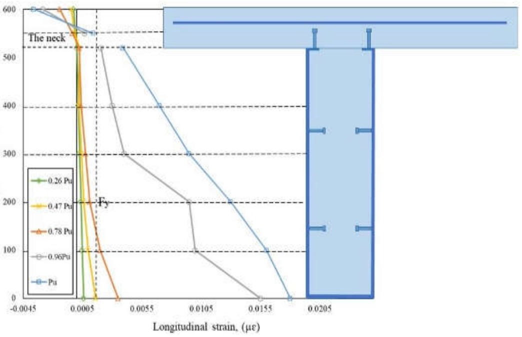

Figure 11: Longitudinal strains distribution alongside for mode 103 H600 b250 t_s80 t_w4 W-SSC

3.3.4 Load-slip relationship.

For the composite section to be as cohesive as feasible and to try to prevent separation between the exterior steel U-section and the encased concrete, the bond between them is crucial. Because of the direct effects of certain parameters, like the coefficient of friction between steel plates and concrete using the side shear connector and also altering the thickness of steel plates, section depth, and beam width, two groups (H400 and H600) were selected to investigate the longitudinal slip behavior. The load-slip curves for these groups, where the slips were measured at the ends of the beams, are shown in figure 12 as well. Using the model (043 H600 b200 t_s80 t_w2 W-SSC) as an example, the load-slip curve shows that the bond between the encased concrete and the external steel U-section exhibited uniform behavior during the elastic zone. Additionally, at a load of 340 kN ($0.5P_u$), the interface slippage between the steel and concrete is nearly 0.08 mm. The slide between the steel and the concrete is still just 0.9 mm as the load value approaches its maximum. The slip value steadily rises after achieving the ultimate load until it deviates from control by 16 mm at the final failure limit.

When comparing the slippage of the several specimens at the maximal load, the following trends are noticed, as shown in figure 13 (1) By employing a side shear connection to increase the coefficient of friction between the concrete and the steel, slippage may be greatly decreased. The steel web experiences local buckling when the composite section is bent. According to the models (043 H600 b200 t_s80 t_w2 W-SSC) and (044 H600 b200 t_s80 t_w2 W/O-SSC), the side shear connection strengthens the bond between the concrete and the steel web at the ultimate load stage and lowers the value of slip by 65%. (2) The absence of side shear connectors and the thickness of steel plates in the model (002 H400 b150 t_s80 t_w2 W/O-SSC) may also limit the slip of steel plates with a thickness of 4 mm (056 H400 b150 t_s80 t_w4 W/O-SSC) by 31% as compared to those with a thickness of 2 mm (002 H400 b150 t_s80 t_w2 W/O-SSC). In contrast to (056 H400 b150 t_s80 t_w4 W/O-SSC), the slip grows more rapidly and local buckling takes place in the steel web once the composite section achieves the highest value. (3) Compared to the model (037 H600 b150 t_s80 t_w2 W-SSC), the slip of the model (013 H400 b250 t_s80 t_w2 W-SSC) rose by 16%. This is mostly because the increased area exposed to friction between the steel web plates and the encased concrete causes the slip to decrease. When the section's depth was extended from 400 mm to 600 mm, the slip decreased by around 17.2%, similar to models (010 H400 b200 t_s100 t_w2 W/O-SSC) and (046 H600 b200 t_s100 t_w2 W/O-SSC). This might be because, as the composite part reaches its ultimate load, the slip is influenced by the deflection values.

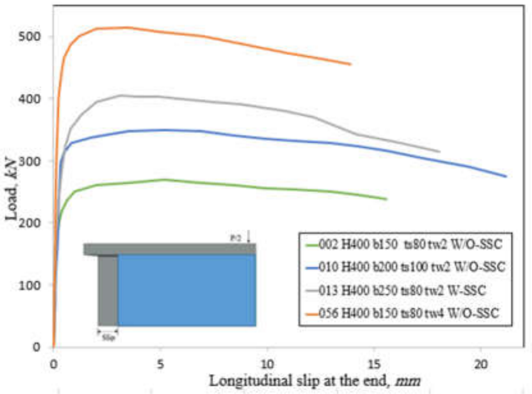

a. Section height 400 mm

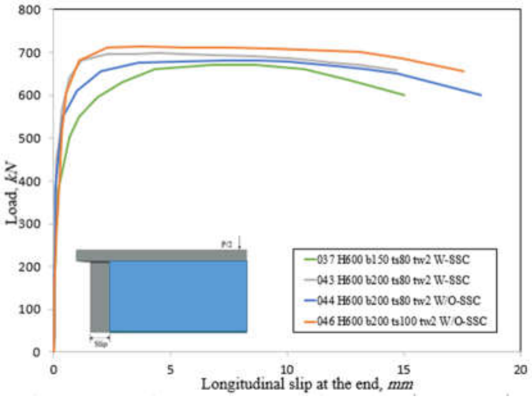

b. Section height 600 mm

Figure 12: Load-slip curves

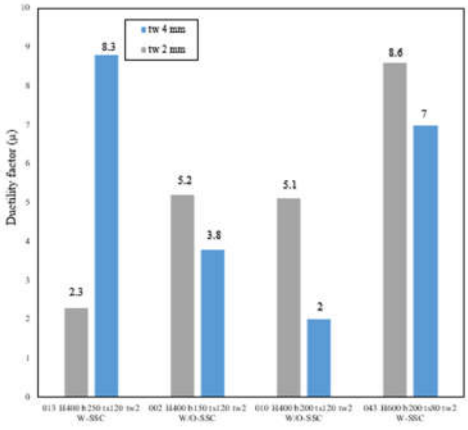

Figure 13: Comparison of slips at peak load values

3.3.5 Ductility

The formula below may be used to define the ductility parameter (μ), which is the primary factor for quantifying structural deformation:

$$\mu = \delta f/\delta y \quad (1)$$

Whereas (δy) denotes the yield deflection when the steel yields, (δf) indicates the mid-span ultimate deflection, which at the stage of decline corresponds to 85% of the peak load. The calculated (μ) values for the 108 specimens, which vary from 17 to 26, are listed in table 4. Figure 14 displays two groups of steel plate specimens with thicknesses of 2 mm and 4 mm. These groups have the following characteristics the thickness of the steel plates used in the U-shaped section is raised from 2 mm to 4 mm, as in models 036 H500 b250 t_s120 t_w2 W/O-SSC and 090 H500 b250 t_s120 t_w4 W/O-SSC, the ductility is enhanced by 15.6%. This is because a steel web that is 2 mm thick is more likely to experience local buckling than one that is 4 mm thick. (2) The 071 H400 b250 t_s120 t_w4 W-SSC side shear connection exhibits superior ductility, 17.4% greater than the 018 H400 b250 t_s120 t_w2 W/O-SSC variant. The reason is that in the absence of side shear connections, the composite action is comparatively weak, and longitudinal slide failure is more likely to occur. (3) Model 101 H600 b200 t_s120 t_w4 W-SSC has a 7.1% higher ductility factor than model 012 H400 b200 t_s120 t_w2 W/O-SSC. Although steel webs that are taller are more likely to buckle than those that are shorter, this is because the steel plates are thicker, have side shear connections, and have the greatest depth. The steel webs are stable as a result of all the above factors. The steel web's height-to-thickness ratio should not exceed 130 to prevent local buckling, provide stability, and improve ductility.

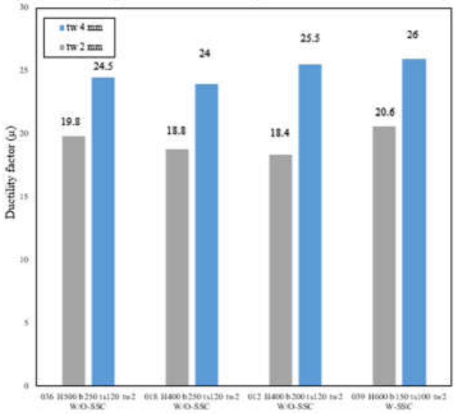

Figure 14: Comparison of ductility factors

3.3.6 Effect of section height

The impact of varying the section height on the PECSB's ultimate load for steel web thicknesses of 2 mm and 4 mm, with or without side shear connections, at the same slab thickness and beam width is shown in figure 15. It was observed that the value of the composite section's ultimate load increased by around 24% when the section height (400 mm) was used for the thicker steel web (4 mm). However, the ultimate load of the composite section increases by around 50% when the section height (600 mm) is used. The explanation is that, in contrast to steel webs with smaller the section height (400 mm), local buckling is observed in steel webs with greater the section height (600 mm). In order to lessen the local buckling that happens in steel webs with a great the section height, it is crucial that the steel web be thicker (4 mm). Regardless of the availability of side shear connections, the PECSB's ultimate load rose by almost 45% when the section height was raised from 400 to 600 mm.

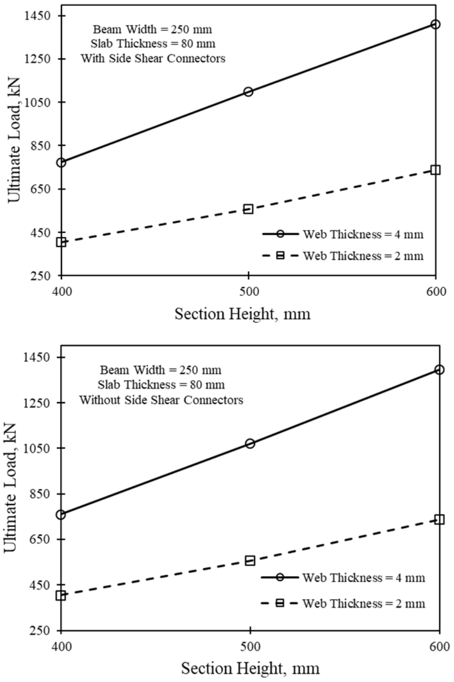

Figure 15: Effect of section height on the ultimate load capacity of the PECSB

3.3.7 Effect of slab thickness

The impact of altering the slab thickness on the PECSB's ultimate load for steel web thicknesses of 2 and 4 mm, with or without side shear connections, at the same section height and the beam width, is shown in figure 16. When the thickness of the slab was increased from 80 to 120 mm, whether or not side shear connectors were available, it was observed that the ultimate load of the composite section increased by a very small amount, approximately 2%, for the larger thickness of the steel web (4 mm). This is because the CBs failed in these cases when longitudinal slips occurred between the concrete and the U-shaped steel section. It was observed that the ultimate load of the CB rose by 10% when the slab thickness was raised from 80 to 100 mm due to fractures in the weak slab concrete, even though the steel web was only 2 mm thick. However, the ultimate load hardly changed when the slab's thickness was raised from 100 to 120 mm, which is why a longitudinal slide between the steel and concrete happened.

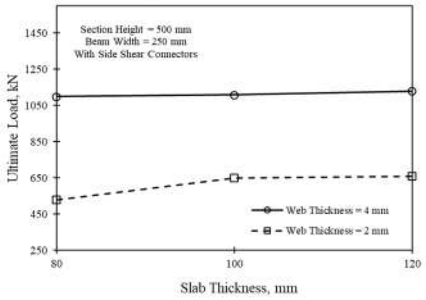

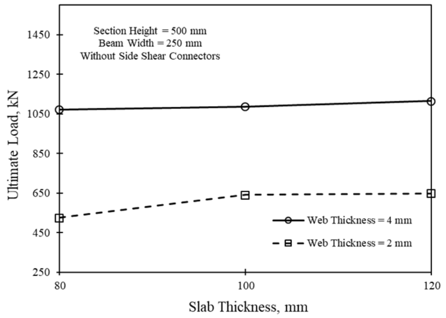

Figure 16: Effect of slab thickness on the ultimate load capacity of the PECSB

3.3.8 Effect of beam width

The impact of altering the beam width on the PECSB's ultimate load for steel web thicknesses of 2 and 4 mm, with or without side shear connections, at the same slab thickness and the section height is depicted in figure 17. It was observed that increasing the steel web thickness from 2 to 4 mm for all beam widths, whether or not side shear connections were accessible, raised the CB's ultimate load by almost 30%. Regardless of whether the steel web was 2 mm or 4 mm, the ultimate load of the CB increased by about 26% when the beam width was increased from 150 mm to 250 mm if side shear connections were utilized. However, when the steel web thickness was 2 mm and the beam width was increased from 150 to 250 mm, the CB's ultimate load increased by over 17%.

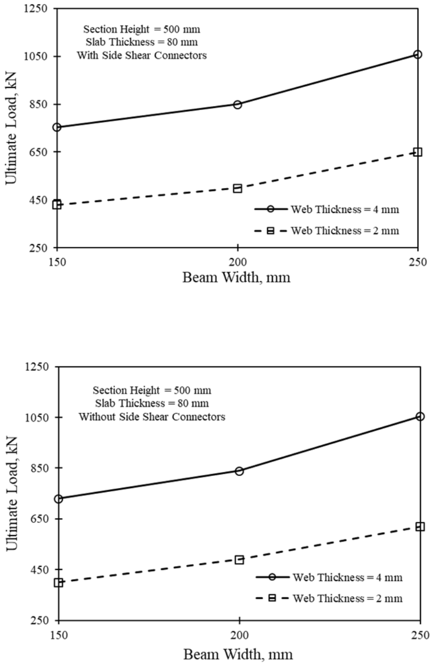

Figure 17: Effect of beam width on the ultimate load capacity of the PECSB

4. COMPARISON BETWEEN FE RESULTS AND EC4 METHOD.

EC4 may be used to determine the bending capacity of the PECSB [18]. Elastic deformation is ignored when the plasticity analysis is taken into account. The computational model shown in figure 18 is predicated on the following assumptions: (1) A linear distribution of stresses results from the cross-section's planes maintaining their original shape after deformation; (2) The rectangular stress block of the concrete slab has the equivalent compressive strength; (3) the U-shaped steel section yields regarding the longitudinal strain distribution for the bottom portion of the section as in section 3.3.3. With a compressive strength of 43 MPa, the tested cubic concrete Fcu may be transformed into prismatic strength ($F_{c,k}$) and cylinder strength ($F_{c,k}$) using the following formula. [18]: $F_{c,k} = F_{cu} \times 0.8 = 43 \times 0.8 = 34.4$ MPa and $F_{c,k} = F_{cu} \times 0.76 = 43 \times 0.76 = 32.7$ MPa; (4) The tensile strength of concrete is disregarded; (5) The PNA is situated in the concrete slab; (6) The slip at the interface between the concrete and steel U-shaped section is disregarded.

According to EC4 [18], the plastic stress distribution in the PECSB cross-section is divided into three zones, as shown in figure 18. The first zone is where the concrete is squeezed on the slab; the second zone is between the first zone and the upper flange of the steel section; and the bottom part of the beam is the third zone. The PNA is regarded as existing inside the concrete slab. Where the depth of the compression area is d_n= $F_{c,k}$ = The concrete's compressive strength = 34.4 MPa; d_c = The distance between the steel section's top flange and the resulting force F_{cc} in the compression region; F_{ys} = The yield strength of the steel section for thicknesses of 2 mm and 4 mm = 326 MPa and 330 MPa, respectively; d_s = The distance between the steel section's resulting tensile force Fss: Therefore, the compressive zone's depth, d_n, is equal to:

$$d_n = \frac{F_{cc}}{B_e \, f'_{c,k}} \tag{2}$$

Since the PNA is present in the concrete slab, the tensile force Fss of the steel section is equivalent to Fcc in the compressive zone:

$$F_{cc}=F_{ss} = b t_w f_{ys} \tag{3}$$

The numbers dc and ds, respectively, reflect the dimensions of Fcc and Fss from the neck and the surface. Consequently, the $M_{(u,E)}$ was computed as follows:

$$M_u^t = F_{cc} \, d_c + F_{ss} \, d_s \tag{4}$$

$$P_u^t = \frac{2M_{u,E}}{L_q} \tag{5}$$

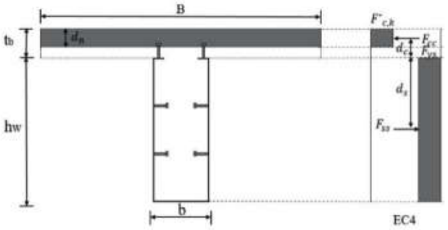

Figure 18: The theoretical model for the bending capacity.

The calculated bending capacity values are summarized in table 4. P_u of the FEA findings and Put by EC4 [18]. With a standard deviation of 0.04, the majority of the calculated values closely match the FEA results. Furthermore, the slab is the best location for the PNA to fully use the steel's tensile strength.

Table 4. The comparison between the theoretical and FEA methods' ultimate loads.

Specimen number	P_u(kN)	P_u^t(kN)	P_u/P_u^t
008 H400 b200 t_s80 t_w2 W/O-SSC	322	340	0.95
010 H400 b200 t_s100 t_w2 W/O-SSC	354	377	0.94
016 H400 b250 t_s100 t_w2 W/O-SSC	411	456	0.91
099 H600 b200 t_s100 t_w4 W-SSC	1337	1343	0.99
103 H600 b250 t_s80 t_w4 W-SSC	1413	1376	1.02
105 H600 b250 t_s100 t_w4 W-SSC	1451	1399	1.03

5. SUMMARY AND CONCLUSION

This work employed the nonlinear FEA approach using the FE analysis to examine the behavior of partly enclosed composite steel beams PECSB under flexural stresses. Using the FEA approach, the investigation research was carried out for Jiepeng et al.'s experimental work [16]. The FEA approach was used in the parametric investigation because of the good agreement between the FEA and the experimental data. In the numerical analysis of the parametric research for PECSB to function as a monolithic unit, the coefficient of friction between concrete and steel is roughly 0.65 and 0.46, respectively, depending on whether side shear connections were used or not—was used from laboratory trials. To create a safe and effective system that employed PECSB for both residential and commercial applications, a parametric analysis was carried out numerically to examine the behavior of 108 FE models of PECSB with various parameters under flexural loads. Lastly, a comparison of the ultimate moment capacity for the theoretical technique according to EC4 [18] and the FEA method was carried out. The following is a summary of the research's findings:

(1) With an accuracy of 96%, the FEA may be used to simulate the experimental work for CBs, greatly cutting down on time, expense, and negligible differences between the FEA and experimental findings.

(2) The PECSB shows three main failure modes: longitudinal slip failure when a small steel ratio in the side shear connectors, especially in the large depth, cannot resist the slip between the encased concrete and the U-shaped steel section; vertical uplift failure at the neck zone between the concrete slab and the top beam of the PECSB when the slab thickness and the steel ratio of the top shear connectors were insufficient to resist the uplift loads; and concrete slab crushing when shear cracks occurred at the sides of the lower part of the PECSB.

(3) Laboratory studies were used to derive the coefficient of friction values between concrete and steel, which were around 0.65 when SSC was used and 0.46 when it wasn't. The slip between the steel and the concrete at the end beam nearly reached 0.9 mm, which was one of the parameters used in the numerical analysis of the parametric research for PECSB to function as a monolithic unit that neared the ultimate load.

(4) Regardless of the availability of side shear connections, the PECSB's ultimate load rose by almost 45% when the section's height was raised from 400 to 600 mm. However, in many instances, the ultimate load rose by almost 17% when the beam width was extended from 150 to 250 mm. Additionally, the ultimate load rose by 10% in several cases when the slab's thickness was extended from 80 to 100 mm, but it hardly changed when it was increased from 100 to 120 mm. The specifications of the PECSB design details were recommended concerning the height-to-thickness ratio of the steel web and the slab width-to-thickness ratio should remain under 130 and 10, respectively, to delay the failures and get a higher ultimate moment capacity.

(5) With excellent deformability, the mid-span deflection reaches $L_o/13$. Additionally, side shear connections can increase the PECSB's ductility factor to 26 with improved ductility and stability.

(6) A comparison of the ultimate load for the FEA method and the theoretical method according to EC4 [18] was conducted with slight differences.

6. NOTATIONS

H	The height of the overall section
B	The breadth of the concrete slab
b	The beam's width
ts	The width of the concrete slab
t_W	The thickness of the U-shaped steel segment
h_W	The U-shaped steel segment web's height
L	The overall span length
L_o	The span of the effective beam
E	The modulus's elasticity
F_{ys}	The steel section's yield strength
F_{cu}	The cubic concrete's measured compressive strength.
$F'_{c,k}$	The cylinder concrete's converted compressive strength.
$F_{c,k}$	The prismatic concrete's converted compressive strength.
F_{cc}	The force responsible for the compression area
F_{ss}	The steel section's resulting tensile force
d_c	The separations between "F" and "cc" from the neck surface
d_s	The separations between "F" and "ss" from the neck surface
d_n	The depth of the compressive zone
My	The bending moment of yield that occurs when the steel soffits
Mu	The experiment's maximum bending moment
Pu	The largest loads
P	The samples were given weights.
M_u^t	The EC4-recommended bending capacity
P_u^t	The peak load was determined using the EC4
δy	The yield load-corresponds to the yield deflection
δf	The final deflection during the descending stage at 85% of the maximum load
μ	The ductility factor for displacement

7. REFERENCES

[1] T.M.Alhajri, M.M. Tahir, et al., Behavior of pre-cast U-shaped CB integrating cold-formed steel with ferro-cement slab, J. Thin-Walled Struct., 102, (2016), 18–29.

[2] Huiyong Ban, Ee Loon Tanc, et al., Strength of multi-span CBs subjected to combined flexure and torsion, J. Constr. Steel Res. 113 (2015) 1–12.

[3] Junli Lyu, Rukai Li, Jian Zhu, et al., Fire resistance of two types of CBs constrained by rigid joint, J. Eng. Struct. 249, (2021), 113337.

[4] B. Uy, M.A. Bradford, Local buckling of cold-formed steel sheeting in profiled CBs at service loads, Struct. Eng. Rev. 7 (4) (1995) 289–300.

[5] B. Uy, M.A. Bradford, Ductility of profiled CBs. Part I: experimental study, J. Struct. Eng. 121 (5) (1995) 876–882.

[6] D.J. Oehlers, Composite profiled beams, J. Struct. Eng. 119 (119) (1995) 407–437.

[7] D.J. Oehlers, H.D. Wright, M.J. Burnet, Flexural strength of profiled beams, J. Struct. Eng. 120 (2) (1994) 378–393.

[8] M. A. Dabaon and Saad Eldeen, Comparison between the theoretical and experimental investigation of CBs with spiral shear connectors, Mansoura Engineering Journal Vol. 20, No. 1, March (1995).

[9] Lanhui Guo, Yong Liu, et al., Fully CBs with U-shaped steel girders: Full-scale tests, computer simulations, and simplified analysis models, J. Eng. Struct. 177 (2018) 724–738.

[10] Liu Y, Guo L, Qu B, Zhang, et al., Experimental investigation on the flexural behavior of steel-concrete CBs with U-shaped steel girders and angle connectors, J. Eng. Struct. (2017), 131:492-502.

[11] Park HG, Hwang HJ, Lee CH, et al., Cyclic loading test for concrete-filled U-shaped steel beam–RC column connections, Eng. Struct. (2012), 36:325-36.

[12] Lee CH, Park HG, Park CH, et al. Cyclic seismic testing of composite concrete-filled U-shaped steel beam to H-shaped column connections, J. Struct. Eng. (2012), 139 (3):360–78.

[13] Q.Y. Shi, B. Ma, A.Q. Li, Experimental study and theoretical analysis of steel encased concrete composite Bbeams, Build. Struct. (8) (2006) 65–68.

[14] Y.C. Zhang, X.Y. Mao, B.Z. Cao, Experimental study and nonlinear FE analysis of lightweight steel-concrete CBs, J. Build. Struct. 24 (1) (2003) 26–33.

[15] S.O. Bamaga, M.M. Tahir, T.C. Tan, et al., Feasibility of developing composite action between concrete and cold-formed steel beam, J. Cent. South Univ. 20 (12) (2013) 3689–3696.

[16] Jiepeng Liu, Yi Zhaoa, Yohchia, et al., Flexural behavior of rebar truss stiffened cold-formed U-shaped steel-concrete CBs, J. Const. Steel Res. 150 (2018) 175–185.

[17] Jiepeng Liu, Yi Zhaoa, Yohchia, et al., Bending experiment on a novel configuration of cold-formed U-shaped steel-concrete CBs, J. Eng. Struct. 180 (2019) 124–133.

[18] EN 1994-1-1. Eurocode 4. Design of composite steel and concrete structures. General rules and rules for buildings. Brussels: European Committee for Standardization; 2005.

[19] American Standard for Testing of Materials; ASTMA370-03a, Standard Test Methods and Definitions for Mechanical Testing of Steel Product, vol.01.04, 2004.

[20] H.Y.Loh, B.Uy, M.A.Bradford, The effects of partial shear connection in composite flush end plate joints Part II Analytical study and design appraisal, J. Constr. Steel Res. 62 (4) (2006) 391- 412.

[21] ECP 203-2020 Egyptian Code for Design and Construction of Reinforced Concrete Structures. National Housing and Building Research Center.

[22] Du, G.F.; Bie, X.M. Study on a constitutive model of shear performance in panel zone of connections composed of CFSSTCs and steel-concrete CBs with external diaphragms. J. Eng. Struct. (2018), 155, 178–191.

[23] Rabbat, B. G., and Russell, H. G., 1985. “Friction coefficients of steel on concrete or grout”. Journal of Structural Engineering, ASCE, Vol. 111, pp. 505-515.